OPEN ACCESS

Impedance of a Hydrogen–Fed SOFC Anode: Analytical and Numerical Models Based on the Dusty Gas Transport Model

To cite this article: Andrei Kulikovsky 2025 *J. Electrochem. Soc.* **172** 074511

Journal of The Electrochemical Society, 2025 **172** 074511

Impedance of a Hydrogen–Fed SOFC Anode: Analytical and Numerical Models Based on the Dusty Gas Transport Model

Andrei Kulikovsky[z]

Forschungszentrum Jülich GmbH Theory and Computation of Energy Materials (IET–3) Institute of Energy and Climate Research, D–52425 Jülich, Germany

Analytical low-current and numerical high–current models for the impedance of a hydrogen–fed anode of an anode–supported button SOFC are developed. The models use the full dusty gas transport model for the binary H_2–H_2O mixture. We show that neglecting the pressure gradient may lead to a severe underestimation of the effective hydrogen diffusivity in the support layer. A least-squares fitting of the analytical model to a literature spectrum of a button cell is demonstrated. The analytical impedance allows to indicate pitfalls when using equivalent circuits with the Warburg finite-length element for fitting experimental spectra. The model parameters include the Knudsen hydrogen diffusivity, hydraulic permeability, porosity/tortuosity ratio of the support layer and the ionic conductivity, double layer capacitance, and HOR Tafel slope of the active layer. All of the above parameters can be obtained by fitting the models to experimental spectra.

 [DOI: 10.1149/1945-7111/aded39]

Manuscript submitted January 18, 2025; revised manuscript received May 20, 2025. Published July 23, 2025.

Nomenclature

List of Symbols

^	Marks the dimensionless local ionic current density
~	Marks the other dimensionless variables
B_0	Hydraulic permeability, m^2
b	Tafel slope, V
d	Mean pore diameter, m
C_{dl}	Double layer volumetric capacitance, F m^{-3}
p_h^{ref}	Reference hydrogen pressure, Pa
p_w^{ref}	Reference water vapor pressure, Pa
D_m	Effective binary H_2–H_2O molecular diffusion coefficient in the ASL, m^2 s^{-1}
D_m^{free}	Binary H_2–H_2O molecular diffusion coefficient in a free space, m^2 s^{-1}
$D_{K,h}$	Effective Knudsen diffusion coefficient of hydrogen, m^2 s^{-1}
E	Dimensionless parameter, Eq. 24
F	Faraday constant, C mol^{-1}
J	DC cell current density, A m^{-2}
j	Local ionic current density, A m^{-2}
K	$=D_{K,h}/D_m$
L	Anode support layer thickness, m
L_{cab}	Cable inductance, H
l_a	Anode active layer thickness, m
M	Molecular weight, kg mol^{-1}
N	Molar flux of hydrogen, mol m^{-2} s^{-1}
P	Dimensionless parameter, Eq. 24
p	Pressure, Pa
p_*	Characteristic pressure, Pa, Eq. 3
q	Dimensionless parameter, Eq. 22
R	Gas constant, J K^{-1} mol^{-1}
R_{tr}	ASL transport resistivity, Ohm cm^2, Eq. 37
R_W	Resistivity, Ohm cm^2, Eq. 33
r_{ref}	Dimensionless parameter, Eq. 22
S_{cell}	Cell active area, m^2
T	Cell temperature, K
W	Dimensionless parameter, Eq. 17
X	Coordinate through the ASL counted from the chamber, m
x	Coordinate through the anode active layer counted from the ASL/AAL interface, m
Y	Dimensionless parameter, Eq. 24
y	Molar fraction of hydrogen
Z	Impedance, Ohm m^2

Subscripts

*	Characteristic value
a	ASL/active layer interface
$anly$	Analytical (impedance)
c	Channel/ASL interface
HFR	High-frequency resistance
h	Hydrogen
K	Knudsen diffusion
RC	Parallel RC–circuit impedance
tr	Transport
m	Molecular diffusion
W	Warburg
w	Water

Superscripts

0	Steady–state value
1	Small–amplitude perturbation
ref	Reference value

Greek

β	Dimensionless parameter, Eq. 21
ε	Dimensionless parameter, Eq. 21
η	HOR overpotential, positive by convention, V
λ	ASL porosity/tortuosity ratio
μ	Mixture dynamic viscosity, Pa s
σ_i	Active layer ionic conductivity, Ω^{-1} m^{-1}
ϕ	Dimensionless parameter, Eq. 31
χ	Dimensionless parameter, Eq. 31
ψ	Dimensionless parameter, Eq. 6
ω	Angular frequency, s^{-1}

Like PEM fuel cells, Solid Oxide Fuel Cells (SOFCs) convert the chemical energy of hydrogen–oxygen combustion directly into electricity. However, unlike PEMFCs, SOFCs operate at high temperature, which allows in–situ conversion of methane to hydrogen and hydrogen to electric power. Most of the households in developed countries have access to methane, which makes the development of a stationary 10–20 kW SOFC power generator a very attractive goal.

[z]E-mail: A.Kulikovsky@fz-juelich.de

Electrochemical impedance spectroscopy (EIS) is, perhaps, the most powerful technique for non–destructive, in-operando analysis and characterization of SOFCs.[1] Impedance spectra contain virtually all information on the transport and kinetic processes inside the cell. However, extracting this information requires quite sophisticated modeling.

A vast majority of works on SOFC impedance spectroscopy employ equivalent circuit models (ECMs).[2–9] The construction of an electrical circuit with an impedance spectrum close to the experimental one is a relatively straightforward procedure leading to fast fitting codes. However, equivalent spectra are not unique and they typically contain constant phase elements with no clear physical meaning. Furthermore, the hydrogen transport in the anode support layer (ASL) is usually described by the Warburg finite-length impedance. However, the Warburg impedance does not take into account the pressure gradient effects in the ASL, nor does it account for the finite double layer capacitance of the active layer, to which the ASL is attached (see below). A strong criticism of ECMs has been made by Macdonald in his seminal paper.[10]

Physics-based impedance models employing classical transient charge and mass conservation equations are free from these drawbacks. There are two ways to calculate impedance from these equations. Applying a small-amplitude harmonic current or potential perturbation at $t = 0$, the transient equations can be solved in the time domain. The impedance is then calculated from a fast Fourier transform of the solution.[11–15] In, Ref. [16] it was suggested calculating impedance by applying a small potential step to the cell rather than a harmonic AC signal. The advantage of this approach is that the entire impedance spectrum can be obtained from a single model run, as the step-like function contains all the necessary frequencies in its Fourier spectrum.

Alternatively, the conservation equations can be directly linearized and Fourier-transformed. In the case of a single spatial dimension, this leads to a system of linear ODEs for the small perturbation amplitudes, which can be solved either numerically,[17,18] or analytically,[19] if possible. Though this approach requires some preliminary analytical work (linearization and Fourier-transform of equations) it results in a much faster numerical code.

Fitting an ECM to an experimental spectrum typically returns the cell resistivities and the DL capacitance. The great advantage of fitting a physics-based model is that it also provides the transport coefficients of the porous media.

Zhu and Kee[12] developed one of the most comprehensive numerical impedance models that takes into account methane reforming in the anode chamber. The transport of gases in the porous layers has been calculated using the full Dusty–Gas Model (DGM), including the pressure gradient term. However, the charge–transfer reactions in the active layers have been described in a simplified manner, using parallel *RC*-circuit elements. Hofmann and Panopoulos[15] calculated the cell impedance from a transient numerical model for SOFC performance based on a commercial CFD solver. Bessler et al.[11] reported the impedance model with the detailed multistep hydrogen oxidation reaction (HOR) mechanism. In their model, the pressure gradient effects in the porous layers were neglected.

Shi et al.[14] developed a one–dimensional through–plane transient model for SOFC performance and calculated the impedance from a time–domain solution. The hydrogen transport through the ASL was described neglecting the pressure gradient. Later, Shi et al.[20] extended their model to two spatial dimensions.

Fu et al.[21] presented analysis of multicomponent diffusion in the porous anode and compared the impedance spectra measured at OCV with the model calculations. The authors[21] claimed that the pressure gradient effects can be neglected if the anode porosity is sufficiently high. However, no criteria for such a neglect have been reported.

Bertei et al.[17] developed a detailed 1d impedance model with the transport properties of the porous layers determined from the microstructural model. Their model included the full DGM for the gaseous transport on both sides of the cell. In another paper, Bertei et al.[22] reported an analytical macro-homogeneous impedance model for the SOFC anode assuming linear kinetics of the faradaic reaction and neglecting pressure gradient effects. The finite-length Warburg terms were derived for hydrogen and water transport in the ASL. The Nernst equation was used to relate the perturbation amplitudes of the overpotential and gas molar fractions. However, the Nernst equation is not valid in non-equilibrium conditions. A rigorous approach based on the ionic charge conservation equation leads to a *RC*–factor in the transport impedance formula (section III B).

Recently, Donazzi et al.[18] reported a 1d+1d impedance model of the SOFC with the straight channel on both sides. The transport in the electrodes was described using a Fick's type relation for the fluxes. The conservation equations were linearized and Fourier-transformed, and the resulting linear ODEs were solved numerically. Knappe and Kulikovsky[19] developed an analytical model for the anode impedance; however, for simplicity, the pressure-gradient driven transport in the ASL was ignored.

From this overview it can be seen that only two works[12,17] have included the pressure gradient effects in the impedance calculations. Both the models[12,17] are numerical and none of the works clarified the role of the pressure gradient in hydrogen transport. The effect of the pressure gradient in the ASL on cell impedance is not fully understood.

In this work, we develop analytical and numerical physics-based models for the anode impedance of an anode-supported SOFC operating on a hydrogen-water mixture. The models employ DGM equations to describe the H_2–H_2O mixture transport in the ASL. The models highlight the effect of the pressure gradient on the anode impedance. The analytical model reveals the pitfalls when using the isobaric Warburg finite–length element in ECMs.

The analytical model is very fast and it can replace the ECMs in fitting low-current spectra, including those measured at OCV. The slower and more complicated numerical model could still be used to fit spectra measured at medium to high DC currents.

Transport and Charge Conservation Equations

The models are based on the following assumptions.

- The hydrogen transport loss in the anode active layer (AAL) is negligible. This assumption is justified as the AAL thickness is typically two orders of magnitude smaller than the support layer thickness (see also discussion in Section IV C).
- The rate of the HOR is described by the Butler–Volmer equation. This is the standard approach in modeling SOFC impedance.
- The variation of the potential of the electronically conducting phase in the anode is ignored, since the electron conductivity of the nickel cermet is usually several orders of magnitude higher, than the ionic conductivity.

Additional assumptions specific to the analytical model are discussed in Section III B.

The transport of hydrogen and water in the ASL is described within the scope of the classical DGM:

$$\sum_{i\neq k}\frac{y_iN_k-y_kN_i}{D_{ik}}+\frac{N_k}{D_{K,k}}=-\frac{p}{RT}\frac{\partial y_k}{\partial X}-\frac{1}{RT}\left(y_k+\frac{y_k}{D_{K,k}}\frac{pB_0}{\mu}\right)\frac{\partial p}{\partial X} \quad [1]$$

Here N_k is the molar flux of the kth component, p the pressure, $D_{i,k}$ the effective binary molecular diffusion coefficient, $D_{K,k}$ the effective Knudsen diffusion coefficient, B_0 the hydraulic permeability of the porous media, μ the mixture kinematic viscosity, and X is the coordinate through the ASL (Fig. 1). The DGM takes into account the inter–diffusion Stefan–Maxwell fluxes (the first term on the left side), the Knudsen diffusion in smaller pores (the second

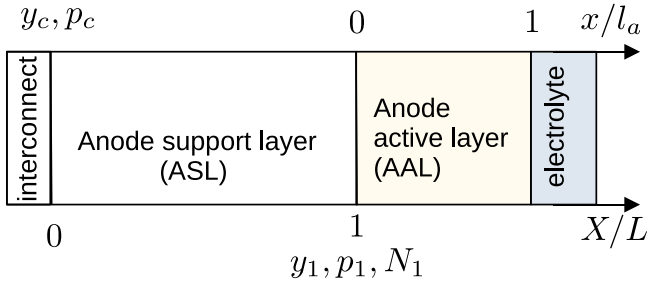

Figure 1. Schematic of the anode–supported SOFC anode. The sketch is strongly not to scale: the active layer thickness is two orders of magnitude smaller than the ASL thickness.

term on the left side), and the flux due to the pressure gradient (the last term in Eq. 1).

Transport equations in the support layer.—No reactions run in the ASL and hence the transient hydrogen mass conservation equation is

$$\frac{1}{RT}\frac{\partial(yp)}{\partial t} + \frac{\partial N}{\partial X} = 0 \qquad [2]$$

where y is the hydrogen molar fraction, N the hydrogen molar flux. Below, the following dimensionless variables will be used

$$\tilde{X} = \frac{X}{L}, \quad \tilde{x} = \frac{x}{l_a}, \quad \tilde{t} = \frac{t}{t_*}, \quad \tilde{p} = \frac{p}{p_*}, \quad \tilde{N} = \frac{N}{N_*},$$
$$\hat{j} = \frac{j}{j_*}, \quad \tilde{J} = \frac{J}{J_*}, \quad \tilde{\eta} = \frac{\eta}{b_h}, \quad \tilde{\omega} = \omega t_*, \quad \tilde{Z} = \frac{Z l_a}{\sigma_i} \qquad [3]$$

where

$$p_* = \frac{\mu D_{K,h}}{B_0}, \quad t_* = \frac{C_{dl} b_h}{i_*},$$
$$N_* = \frac{\mu D_{K,h}^2}{RTLB_0}, \quad j_* = \frac{\sigma_i b_h}{l_a}, \quad J_* = 2FN_*, \qquad [4]$$

x is the coordinate through the active layer (Fig. 1), L the ASL thickness, l_a is the AAL thickness, J the cell current density, η the positive by convention HOR overpotential, b_h the HOR Tafel slope, $D_{K,h}$ the Knudsen hydrogen diffusivity in the ASL, C_{dl} the double layer volumetric capacitance, i_* the HOR volumetric exchange current density, σ_i the AAL ionic conductivity, ω the angular frequency, and Z the impedance.

With these variables, Eq. 2 takes the form

$$\frac{\partial(y\tilde{p})}{\partial\tilde{t}} + \psi^2\frac{\partial\tilde{N}}{\partial\tilde{X}} = 0, \qquad [5]$$

where

$$\psi = \sqrt{\frac{C_{dl} b D_{K,h}}{i_* L^2}}. \qquad [6]$$

The dimensionless DGM equations for y and $\tilde{p}$ in the binary H_2–H_2O mixture are:[23]

$$\frac{\partial(y\tilde{p})}{\partial\tilde{X}} + y\tilde{p}\frac{\partial\tilde{p}}{\partial\tilde{X}} = -(1+K)\tilde{N} \qquad [7]$$

$$(1 + \tilde{p}\,(3-2y))\frac{\partial\tilde{p}}{\partial\tilde{X}} = 2\tilde{N} \qquad [8]$$

where

$$K = \frac{D_{K,h}}{D_m} \qquad [9]$$

and D_m is the effective molecular diffusion coefficient of the H_2–H_2O mixture in the ASL. Equation 7 is the dimensionless DGM Eq. 1 for the hydrogen molar fraction. Equation 8 is the sum of Eq. 1 for the hydrogen y and water y_w molar fractions, taking into account that $y_w = 1 - y$ and the water molar flux $N_w = -N$.

Application of the small–amplitude harmonic AC current to the cell induces the small–amplitude response of all transport variables. Equations for this response can be derived by linearization and Fourier–transform of Eqs. 5, 7 and 8 using the substitutions

$$y = y^0(\tilde{X}) + y^1(\tilde{X},\tilde{\omega})\exp(\mathrm{i}\tilde{\omega}\tilde{t}), \quad |y^1| \ll y^0$$
$$\tilde{p} = \tilde{p}^0(\tilde{X}) + \tilde{p}^1(\tilde{X},\tilde{\omega})\exp(\mathrm{i}\tilde{\omega}\tilde{t}), \quad |\tilde{p}^1| \ll \tilde{p}^0$$
$$\tilde{N} = \tilde{N}^0(\tilde{X}) + \tilde{N}^1(\tilde{X},\tilde{\omega})\exp(\mathrm{i}\tilde{\omega}\tilde{t}), \quad |\tilde{N}^1| \ll \tilde{N}^0 \qquad [10]$$

where the superscripts 0 and 1 mark the static variables and the small perturbation amplitudes, respectively. Note that y^1, $\tilde{p}^1$ and $\tilde{N}^1$ are the perturbation amplitudes in the $\tilde{\omega}$–space. Neglecting terms with the perturbations product and subtracting the respective static equations we come to

$$\psi^2\frac{\partial\tilde{N}^1}{\partial\tilde{X}} = -(\tilde{p}^0 y^1 + y^0\tilde{p}^1)\mathrm{i}\tilde{\omega}, \qquad [11]$$

$$\tilde{p}^0\frac{\partial y^1}{\partial\tilde{X}} + \tilde{p}^1\frac{\partial y^0}{\partial\tilde{X}} + (y^0\tilde{p}^1 + y^1(1+\tilde{p}^0))\frac{\partial\tilde{p}^0}{\partial\tilde{X}}$$
$$+ y^0(1+\tilde{p}^0)\frac{\partial\tilde{p}^1}{\partial\tilde{X}} = -(1+K)\tilde{N}^1 \qquad [12]$$

$$(3\tilde{p}^1 - 2(\tilde{p}^0 y^1 + \tilde{p}^1 y^0))\frac{\partial\tilde{p}^0}{\partial\tilde{X}} + (1 + \tilde{p}^0(3-2y^0))\frac{\partial\tilde{p}^1}{\partial\tilde{X}} = 2\tilde{N}^1 \qquad [13]$$

Multiplying Eq. 12 by 2 and summing with Eq. 13, we get a more compact equation for $\partial y^1/\partial\tilde{X}$:

$$2\tilde{p}^0\frac{\partial y^1}{\partial\tilde{X}} + 2\tilde{p}^1\frac{\partial y^0}{\partial\tilde{X}} + (2y^1 + 3\tilde{p}^1)\frac{\partial\tilde{p}^0}{\partial\tilde{X}}$$
$$+ (1 + 2y^0 + 3\tilde{p}^0)\frac{\partial\tilde{p}^1}{\partial\tilde{X}} = -2K\tilde{N}^1 \qquad [14]$$

For the static shapes y^0 and $\tilde{p}^0$ we use the approximate analytical solutions to the system 7, 8:[23]

$$y^0 = \frac{1}{\tilde{p}_c^0 + W\tilde{X}}\left(y_c\tilde{p}_c^0 - \frac{3}{4}W^2\tilde{X}^2 - \left(\frac{(3\tilde{p}_c^0+1)}{2}W + K\tilde{J}\right)\tilde{X}\right) \qquad [15]$$

$$\tilde{p}^0 = \tilde{p}_c^0 + W\tilde{X} \qquad [16]$$

where y_c, $\tilde{p}_c$ are the the hydrogen molar fraction and dimensionless pressure in the anode chamber, and

$$W = \frac{2\tilde{J}}{1 + \tilde{p}_c(3-2y_c)}. \qquad [17]$$

The derivative $\partial y^0/\partial\tilde{X}$ is given by Eq. B.2 and $\partial\tilde{p}^0/\partial\tilde{X} = W$.

The boundary conditions for Eqs. 11, 13, 14 are

$$\tilde{p}^1(0) = y^1(0) = 0, \quad \tilde{N}^1(0) = \tilde{J}^1 \tag{18}$$

The first two conditions express unperturbed pressure and hydrogen molar fraction in the anode channel and the last one means that $\tilde{N}^1(0)$ is equal to the applied current density perturbation $\tilde{J}^1$. The system of Eqs. 11, 13, 14 with the boundary conditions 18 form a linear initial–value (Cauchy) problem for $\tilde{N}^1$, y^1 and $\tilde{p}^1$ in the ASL.

Ionic charge conservation in the active layer.—Due to the small AAL thickness, we neglect the variation of hydrogen and water concentrations through the AAL depth. The ionic charge conservation equation in the AAL is

$$C_{dl}\frac{\partial \eta}{\partial t} - \sigma_i \frac{\partial^2 \eta}{\partial x^2} = -i_*\left(\frac{p_h}{p_h^{ref}}\exp\left(\frac{\eta}{b_h}\right) - \frac{p_w}{p_w^{ref}}\exp\left(-\frac{\eta}{b_w}\right)\right) \tag{19}$$

where σ_i is the AAL ionic conductivity, b_w the Tafel slope of the hydrogen evolution reaction (HER), p_h and p_w are the hydrogen and water partial pressures, respectively, and p_h^{ref}, p_w^{ref} the reference pressures. The right side is the Butler–Volmer reaction rate, where the first exponent describes the direct HOR rate and the second exponent represents the rate of the reverse HER.

With the dimensionless variables Eqs. 3, Eq.19 takes the form

$$\frac{\partial \tilde{\eta}}{\partial \tilde{t}} - \varepsilon^2 \frac{\partial^2 \tilde{\eta}}{\partial \tilde{x}^2} = -q\tilde{p}\,(y\exp(\tilde{\eta}) - r_{ref}(1-y)\exp(-\beta\tilde{\eta})) = -qQ. \tag{20}$$

Here β, ε, q and r_{ref} are the constant parameters:

$$\beta = \frac{b_h}{b_w}, \quad \varepsilon = \sqrt{\frac{\sigma_i b_h}{i_* l_a^2}} \tag{21}$$

$$q = \frac{\mu D_{K,h}}{B_0 p_{h,ref}}, \quad r_{ref} = \frac{p_{h,ref}}{p_{w,ref}}. \tag{22}$$

Linearization of the factor Q in Eq. 20 gives

$$Q^1 = Yy^1 + P\tilde{p}^1 + E\tilde{\eta}^1 \tag{23}$$

where

$$\begin{aligned} Y &= \tilde{p}^0(\exp(\tilde{\eta}^0) + r_{ref}\exp(-\beta\tilde{\eta}^0)) \\ P &= y^0\exp(\tilde{\eta}^0) - r_{ref}\exp(-\beta\tilde{\eta}^0)(1-y^0) \\ E &= \tilde{p}^0(y^0\exp(\tilde{\eta}^0) + r_{ref}\beta\exp(-\beta\tilde{\eta}^0)(1-y^0)) \end{aligned} \tag{24}$$

Substituting into Eq. 20 the Fourier–transform

$$\tilde{\eta} = \tilde{\eta}^0(\tilde{x}) + \tilde{\eta}^1(\tilde{x},\tilde{\omega})\exp(\mathrm{i}\tilde{\omega}\tilde{t}), \quad |\tilde{\eta}^1| \ll \tilde{\eta}^0 \tag{25}$$

expanding exponents, neglecting the terms with perturbation product and subtracting the static equation for $\tilde{\eta}^0$, we get the problem for the overpotential perturbation amplitude $\tilde{\eta}^1$:

$$\begin{aligned} &\varepsilon^2\frac{\partial^2\tilde{\eta}^1}{\partial\tilde{x}^2} = (\mathrm{i}\tilde{\omega} + qE_1)\tilde{\eta}^1 + q(Y_1 y_1^1 + P_1\tilde{p}_1^1), \\ &\left.\frac{\partial\tilde{\eta}^1}{\partial\tilde{x}}\right|_{\tilde{x}=0} = 0, \quad \left.\frac{\partial\tilde{\eta}^1}{\partial\tilde{x}}\right|_{\tilde{x}=1} = \hat{j}_1^1 \end{aligned} \tag{26}$$

The terms $Y_1 y_1^1$ and $P_1\tilde{p}_1^1$ in Eq. 26 include solutions y_1^1 and $\tilde{p}_1^1$ of the problem 11, 13, 14 calculated at the ASL/AAL interface (at $\tilde{X} = 1$). The factors Y_1, P_1 and E_1 are given by Eq. 24 with the static parameters y_1^0, $\tilde{p}_1^0$ calculated at $\tilde{X} = 1$.

The left boundary condition in Eq. 26 means zero ionic current through the ASL/AAL interface ($\tilde{x} = 0$). The parameter $\hat{j}^1$ in the right boundary condition is the ionic current density equivalent to the stoichiometric hydrogen flux entering the AAL/ASL interface

$$\hat{j}^1 = \frac{J_*\tilde{N}_1^1}{j_*} \tag{27}$$

Note that $\hat{j}^1$ is scaled to satisfy the Ohm's law in the form of $\hat{j} = \partial\tilde{\eta}/\partial\tilde{x}$ used in Eq. 20 and in the boundary condition to Eq. 26.

Impedance Models

Numerical impedance model.—A high–current numerical anode impedance Z_{num} is calculated taking into account the variation of the pressure and hydrogen concentration through the ASL and the variation of the static overpotential $\tilde{\eta}^0$ along $\tilde{x}$ due to the finite ionic conductivity. The procedure is as follows.

1. Fix the static cell current density $\tilde{J}^0$ and solve the system 11, 13, 14 with the boundary conditions Eq. 18 and with the static shapes $y^0(\tilde{X})$ and $\tilde{p}^0(\tilde{X})$ given by Eqs. 15, 16.
2. Solve the static problem for $\tilde{\eta}^0(\tilde{x})$:

$$\begin{aligned} &\varepsilon^2\frac{\partial^2\tilde{\eta}^0}{\partial\tilde{x}^2} = q\tilde{p}_1^0\,(y_1^0\exp(\tilde{\eta}^0) - r_{ref}(1-y_1^0)\exp(-\beta\tilde{\eta}^0)), \\ &\left.\frac{\partial\tilde{\eta}^0}{\partial\tilde{x}}\right|_{\tilde{x}=0} = 0, \quad \left.\frac{\partial\tilde{\eta}^0}{\partial\tilde{x}}\right|_{\tilde{x}=1} = \tilde{J}_0\frac{J_*}{j_*} \end{aligned} \tag{28}$$

3. Solve the problem for $\tilde{\eta}^1$, Eq. 26, with Y, P and E from Eqs. 24 and $\tilde{\eta}^0(\tilde{x})$ from the previous step.
4. Calculate the numerical impedance

$$\tilde{Z}_{num} = \left.\frac{\tilde{\eta}^1}{\partial\tilde{\eta}^1/\partial\tilde{x}}\right|_{\tilde{x}=1}. \tag{29}$$

Analytical low-current impedance model.—When the DC current is small, we can neglect the variation of the static pressure $\tilde{p}^0$ and hydrogen concentration y^0 through the ASL depth, but keep the perturbation amplitudes y^1, $\tilde{p}^1$, and $\tilde{N}^1$ as functions of $\tilde{X}$. The static overpotential $\tilde{\eta}^0$ can also be approximated by a constant value. Under these assumptions, the analytical anode impedance $\tilde{Z}_{anly}$ can be derived (Appendix A)

$$\tilde{Z}_{anly} = \frac{1}{\phi\tanh\phi} + \frac{\chi\tilde{R}_W\tanh\left(\sqrt{\mathrm{i}\tilde{\omega}\xi/\psi^2}\right)}{(\mathrm{i}\tilde{\omega} + qE_1)\sqrt{\mathrm{i}\tilde{\omega}\xi/\psi^2}} \tag{30}$$

where

$$\phi = \frac{\sqrt{\mathrm{i}\tilde{\omega} + qE_1}}{\varepsilon}, \quad \chi = \frac{qj_*}{J_*}, \tag{31}$$

$$\xi = \frac{((3-2y_c)K + 3)\tilde{p}_c + K + 1}{1 + \tilde{p}_c(3-2y_c)}, \tag{32}$$

ψ is given in Eq. 6, and

$$\tilde{R}_W = \frac{Y_1\xi}{\tilde{p}_c} + \frac{2(Y_1 y_c - P_1\tilde{p}_c)}{(1+\tilde{p}_c(3-2y_c))\tilde{p}_c} \quad [33]$$

(see also Table I for the dimensionless parameters).

The first term in Eq. 30 is the combined faradaic and ionic transport impedance of the AAL. The second therm in Eq. 30 is the ASL transport impedance

$$\tilde{Z}_{tr} = \frac{\chi\tilde{R}_W \tanh\left(\sqrt{\mathrm{i}\tilde{\omega}\xi/\psi^2}\right)}{(\mathrm{i}\tilde{\omega} + qE_1)\sqrt{\mathrm{i}\tilde{\omega}\xi/\psi^2}}, \quad [34]$$

given by the product of the Warburg-like finite-length impedance

$$\tilde{Z}_W = \frac{\chi\tilde{R}_W \tanh\left(\sqrt{\mathrm{i}\tilde{\omega}\xi/\psi^2}\right)}{\sqrt{\mathrm{i}\tilde{\omega}\xi/\psi^2}} \quad [35]$$

and the parallel *RC*-circuit impedance

$$\tilde{Z}_{RC} = \frac{1}{\mathrm{i}\tilde{\omega} + qE_1} \quad [36]$$

where $\tilde{R} \sim 1/(qE_1)$ is the faradaic resistance. The *RC*-factor arises since the transport layer (in this context, the ASL) is attached to the porous active layer with the finite double layer capacitance. This capacitance (and the displacement current) were ignored by Warburg in his classic derivation of the semi–infinite transport layer impedance[24] and later in the derivation of the Warburg finite-length impedance. Note that the presence of the *RC*-factor is independent of the pressure gradient value.

It can be shown that in the limit of $C_{dl} \to 0$, Eq. 34 reduces to the Warburg impedance. Indeed, in Eq. 34, the ratio $\tilde{\omega}/\psi^2$, and the factors χ, q, E_1, $\tilde{R}_W$ are all independent of C_{dl}. The only term proportional to C_{dl} is $\mathrm{i}\tilde{\omega}$ in the denominator of Eq. 34. Thus, at $C_{dl} \to 0$ the *RC*–impedance reduces to the constant real value $1/(qE_1)$ and Eq. 34 transforms to the scaled Warburg impedance $\tilde{Z}_W/(qE_1)$ (see[25] for further discussions).

In the limit of $\omega \to 0$, the factor $\tanh\left(\sqrt{\mathrm{i}\tilde{\omega}\xi/\psi^2}\right)/\sqrt{\mathrm{i}\tilde{\omega}\xi/\psi^2} \to 1$ and from Eq. 34 we get the anode transport resistivity $\tilde{R}_{tr}$ at low cell current density

$$\tilde{R}_{tr} = \frac{\chi\tilde{R}_W}{qE_1} = \frac{j_*\tilde{R}_W}{J_*E_1} \quad [37]$$

Dimension formulas for R_{tr} and Z_{anly} can be obtained from Eqs. 37 and 30, respectively, using the list of the dimensionless parameters and variables in Table I.

Table I. The dimensionless variables and parameters in alphabetic order.

$j_* = \sigma_i b_h/l_a$
$\tilde{J} = J/J_*, \quad J_* = 2F\mu D_{K,h}^2/(RTLB_0)$
$\hat{j} = j/j_*, \quad j_* = \sigma_i b_h/l_a$
$K = D_{K,h}/D_m$
$\tilde{N} = N/N_*, \quad N_* = \mu D_{K,h}^2/(RTLB_0)$
$\tilde{p} = p/p_*, \quad p_* = \mu D_{K,h}/B_0$
$q = \mu D_{K,h}/(B_0 p_h^{ref})$
$\tilde{R}_{tr} = R_{tr} l_a/\sigma_i$
$r_{ref} = p_h^{ref}/p_w^{ref}$
$\tilde{t} = t/t_*, \quad t_* = C_{dl} b_h/i_*$
$\tilde{X} = X/L$
$\tilde{x} = x/l_a$
Y_1, P_1, E_1, Eq. 24 where $\tilde{p}^0 = \tilde{p}_1^0$, $y^0 = y_1^0$, for the numerical model, or $\tilde{p}^0 = \tilde{p}_c$, $y^0 = y_c$ for the analytical model
$\tilde{Z} = Z\sigma_i/l_a$

$\alpha = RT/(b_h F)$
$\beta = b_h/b_w = 1/3$
$\varepsilon = \sqrt{\sigma_i b_h/(i_* l_a^2)}$
$\tilde{\eta} = \eta/b_h$
$\tilde{\eta}^0$ Solution to Eq. 28 (numerical model), or solution to Eq. A.2 (analytical model)
$\xi = (((3-2y_c)K+3)\tilde{p}_c + K + 1)/(1+\tilde{p}_c(3-2y_c))$
$\phi = \sqrt{\mathrm{i}\tilde{\omega} + qE_1}/\varepsilon$
$\chi = RTL\sigma_i b_h/(2FD_{K,h}p_h^{ref} l_a)$
$\psi = \sqrt{C_{dl} b_h D_{K,h}/(i_* L^2)}$
$\tilde{\omega} = \omega C_{dl} b_h/i_*$

Numerical Results and Discussion

Model spectra.—Numerical calculations have been performed using a custom Python code. Equations. 11, 13, 14 with the boundary conditions 18 form a complex-valued Cauchy problem, which has been solved by the standard Runge–Kutta *solve_ivp* solver. The current–voltage relation, Eq. A.2 has been solved using the *fsolve* procedure. Equation 28 for the static overpotential, and the system of real and imaginary parts of Eq. 26 for the overpotential perturbation amplitude are the boundary–value problems, which have been solved using the BVP *solve_bvp* solver. Regrettably, *solve_bvp* fails to directly solve the complex–valued BVP Eq. 26 for sufficiently high frequencies.

The transport coefficients have been calculated from Eq. B.1. The cell parameters taken from the literature are listed in Table II. Comparison of the analytical low-current impedance, Eq. 30, with the numerical one is shown in Fig. 2. Both the impedances are calculated at the small current density of 1 mA cm^{-2}, which mimics the electronic leakage current density in the cell at OCV. As can be seen, the analytical and the exact numerical spectra are indistinguishable.

Fig. 3 shows the numerical and analytical model spectra for the cell current density of 20 mA cm^{-2} and the set of parameters in Table II. The analytical model quite well describes the exact numerical spectrum up to 20 mA cm^{-2}. Equation 30 can thus be used for fast fitting the impedance spectra measured at low currents, down to OCV conditions. Eq. 37 can be used for calculation of the anode transport resistivity R_{tr}.

The numerical model allows to rationalize the effect of pressure gradient on the anode impedance. For this purpose, the terms with $\tilde{p}^1$, $\partial\tilde{p}^1/\partial\tilde{x}$ and $\partial\tilde{p}^0/\partial\tilde{x}$ have been set to zero. The reduced numerical model describes the isobaric anode impedance with purely diffusive hydrogen transport through the ASL.

The resulting spectra are shown in Fig. 4. A comparison of Figs. 3 and 4 shows that in spite of the low current density, the effect of the finite pressure gradient on the spectrum is quite significant: at zero $\partial p/\partial x$, the transport arc becomes more than twice smaller (cf. Figs. 3a and 4a). In other words, a zero pressure gradient leads to lower transport resistivity. Physically, the finite pressure gradient induces the counterflow of hydrogen toward the anode chamber. Note that the peak of the transport arc imaginary part in Fig. 4b is shifted to twice higher frequency as compared to Fig. 3b. Both the changes could be "corrected" in the isobaric model by using twice lower effective hydrogen diffusivity in the ASL. In other words, fitting the isobaric impedance model to the experimental spectra could give a greatly underestimated effective ASL hydrogen diffusivity.

Fig. 5 shows the ASL transport resistivity R_{tr} calculated from the full DGM and from the isobaric DGM vs the mean pore diameter d

Table II. The cell parameters used in the calculations.

Cell temperature, K	T	$273 + 800$
Pressure in the anode chamber, Pa	p_c	10^5
Current density, A m^{-2}	J	$(20 \cdot 10^{-3}) \cdot 10^4$
ASL thickness, m	L	$10^3 \cdot 10^{-6}$
AAL thickness, m	l_a	$15 \cdot 10^{-6}$
Mean pore diameter, m	d	$0.96 \cdot 10^{-6}$ [26]
Porosity/tortuosity ratio	λ	0.033, [27]
AAL ionic conductivity@800°C, S m^{-1}	σ_i	0.1
Double layer capacitance, F m^{-3}	C_{dl}	$2 \cdot 10^6$
HOR exchange current density A m^{-3}	i_*	10^8
HOR Tafel slope, V/exp	b_h	0.1
Parameter $\beta = b_h/b_w$	β	1/3, [28]
Reference H_2 pressure,	p_h^{ref}	$0.125p_c$
Reference water pressure	p_w^{ref}	$0.042p_c$
Hydrogen viscosity@800°C, Pa s	μ	$2 \cdot 10^{-5}$
H_2/H_2O molecular diffusivity m^2 s^{-1}	D_m^{free}	$8.154 \cdot 10^{-4}$, [27]
Anode chamber gas composition		85%H_2 + 15%H_2O

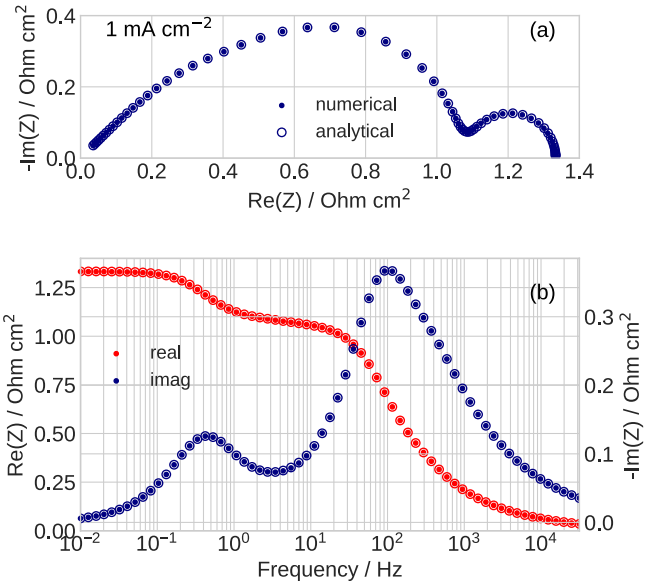

Figure 2. (a) The Nyquist spectra of the numerical anode impedance, Eq. 29, (solid points), and the analytical impedance, Eq. 30, (open circles) for the cell current density of 1 mA cm^{-2}. The other parameters are listed in Table II. (b) The Bode plots of the real and imaginary parts of impedance in (a).

in the ASL. As can be seen, the full DGM shows the strong effect of d on R_{tr}, while the approximation of zero pressure gradient makes R_{tr} practically insensitive to d. Again we note that any point on the full DGM curve in Fig. 5 could be obtained within the scope of the isobaric DGM by lowering the ASL hydrogen diffusivities, i.e., the parameters $D_{K,h}$ and/or D_m derived from the isobaric model could be underestimated.

Fitting the experimental spectrum.—The majority of papers in the field present experimental Nyquist spectra; however, they do not include the complete impedance data necessary for fitting. Ideally, the frequency dependence of the real and imaginary parts should be demonstrated. The work of Shi et al.[14] is one of the very few papers, where the necessary data are reported. To demonstrate the analytical model at work, it has been fitted to the impedance spectrum of the anode–supported button cell measured by Shi et al..[14]

The spectrum in Ref. [14] was acquired at open–circuit and the operating conditions collected in Table III. To describe the high–-frequency features of the spectrum, the following model impedance Z_a has been fitted to the experiment:

$$Z_a = \frac{l_a}{\sigma_i}\tilde{Z}_{anly} + \mathrm{i}\omega L_{cab} S_{cell} + R_{HFR} \qquad [38]$$

where $\tilde{Z}_{anly}$ is given by Eq. 30, L_{cab} the cable inductance, S_{cell} the cell active area, and R_{HFR} the high–frequency cell resistivity. The cathode impedance has been neglected.[17] The fitting has been performed using the Python constrained *least_squares* procedure.

The quality of the spectrum fitting is not high; however, the model correctly captures the faradaic and transport peaks (Fig. 6). The fitting parameters are listed in Table IV. All the anode parameters are close to their literature values (see discussion in.[19]) The present model returns the estimate for the porosity/tortuosity ratio $\lambda \simeq 0.076$ (Table IV), which is nearly twice the value of 0.043 following from the data reported by Shi et al..[14] It should be noted that the parameters b_h, r_{ref} and porosity/tortuosity ratio strongly depend on the HOR exchange current density i_*. The latter has been fixed here using Eq. 39:[6]

$$i_* = \frac{\gamma}{l_a} y_c^a (1 - y_c)^b \exp\left(-\frac{E_{act}}{RT}\right), \ \mathrm{A\ m^{-3}} \qquad [39]$$

where $\gamma = 1.83 \cdot 10^6 T$, $a = -0.1$, $b = 0.33$, $E_{act} = 105.04$ kJ mol^{-1}.

Unfortunately, both i_* and the Tafel slope b_h cannot be included in the list of fitting parameters; one of these parameters must be fixed. Alternatively, b_h could be fixed, and then i_* could be determined from the fitting. Ultimately, more spectra measured at different cell current densities are needed to determine the model parameters more accurately. The results presented in Table IV should be considered as estimates. The spectrum in Fig. 6 could, of course, be fitted using the numerical model. In this case, the Python code runtime is about 33 s on a standard notebook, which is three orders of magnitude larger than the fitting with the analytical model.

The fitted spectrum in Fig. 6a is close to the spectrum reported by Shi et al.[14] from their much more detailed model (cf. Fig. 6a and Fig. 6a in. Ref. [14]) Shi et al. attributed the difference between the experimental and fitted spectra to the effects of diffusion limitations in the anode chamber and in the nickel felt, '...which eventually affected the gas diffusion from the gas chamber to the anode surface'.

Pitfalls when using the Warburg finite-length element.—The Warburg finite-length element has been widely used in ECMs for fitting the impedance spectra[6,7,30] (see also a review[9] and the references therein). The analytical model, Eqs. 30 and 40 below enable to indicate possible pitfalls when using this element. The condition for neglecting the pressure gradient in the ASL is:[23]

$$\frac{JRTL}{FD_{K,h}\left(1 + \frac{p_c B_0 (3 - 2y_c)}{\mu D_{K,h}}\right) p_c} \ll 1 \qquad [40]$$

where y_c, p_c are the hydrogen molar fraction and total pressure, respectively, in the channel. Under this condition, the pressure growth toward the active layer produced by the Knudsen diffusion and/or due to the finite hydraulic permeability of the porous media can be neglected.

At low to medium frequencies, the transport term in Eq. 30 is close to the Warburg finite-length impedance (Fig. 7). Thus, the Warburg element can be safely used to determine the transport resistivity. However, if Eq. 40 does not hold, it is impossible to extract a correct ASL hydrogen diffusivity from the Warburg element.

Further, the active layer ionic conductivity σ_i manifests itself in the high–frequency part of the impedance spectrum. The characteristic frequency f_i of ionic transport in the active layer is[31]

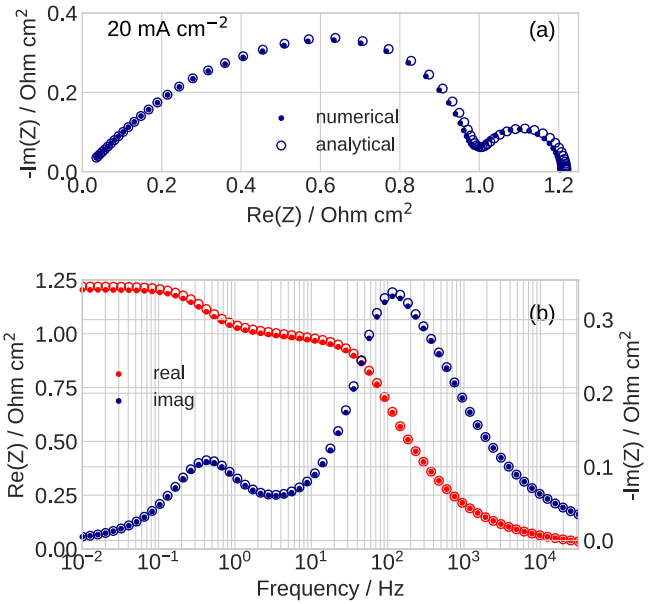

Figure 3. (a) The Nyquist spectra of the numerical anode impedance, Eq. 29, (solid points), and the analytical impedance, Eq. 30, (open circles) for the current density of 20 mA cm^{-2} and the cell parameters in Table II. (b) The Bode plots of the real and imaginary parts of impedance in (a).

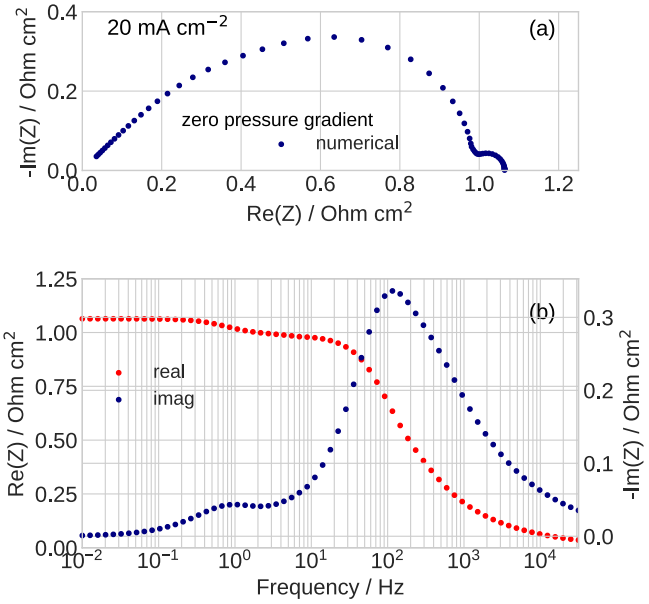

Figure 4. (a) The Nyquist spectrum of the numerical anode impedance, Eq. 29, corresponding to the zero pressure gradient in the anode. The current density is 20 mA cm^{-2} and the cell parameters are listed in in Table II. (b) The Bode plots of the real and imaginary parts of impedance in (a).

$$f_i = \frac{1.71\sigma_i}{C_{dl} l_a^2}, \quad \text{Hz.} \qquad [41]$$

With the parameters from Table II, $f_i \simeq 400$ Hz. The high–frequency behavior of the Warburg impedance and the transport term in Eq. 30 are very different (Fig. 7), and using the Warburg element may return incorrect σ_i.

To summarize,

- The Warburg finite-length element can be safely used to derive the static transport resistivity.

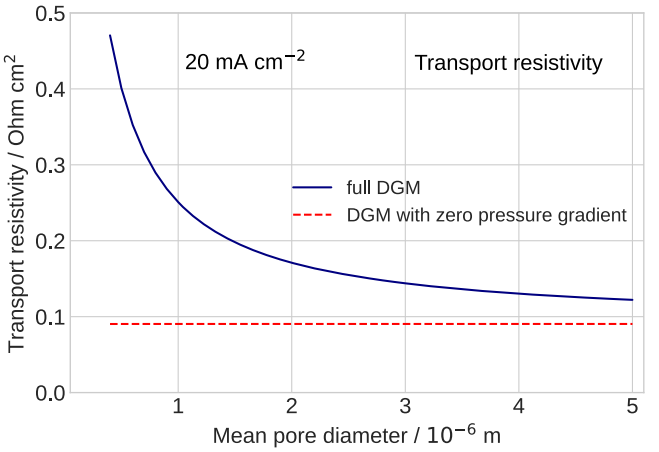

Figure 5. The dependence of transport resistivity on the mean pore diameter in the ASL. Solid line—the full DGM, dashed line—the reduced DGM with the zero pressure gradient.

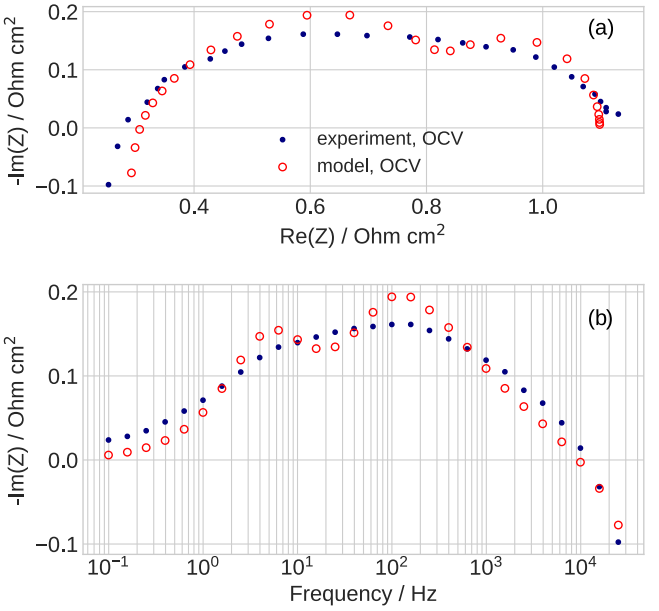

Figure 6. (a) The experimental (solid points) and fitted analytical model, Eq. 30, (open circles) Nyquist spectra of a button SOFC at open–circuit potential. The experimental points are digitized from Figure 6 of Shi et al..[14] The cell operating parameters are listed in Table III. (b) The Bode plot of imaginary part of impedance in (a).

Table III. The working cell parameters reported by Shi et al.[14,29]

Cell temperature T, K	273 + 800
Total anode pressure p, kPa	101.325
Hydrogen partial pressure p_h,	0.958p
Reference H_2 pressure, $p_{h,ref}$	0.125p
Water vapor partial pressure p_w	0.042p
Reference water pressure $p_{w,ref}$	0.042p
ASL thickness L, μm	680
AAL thickness l_a, μm	15
Cell active area, S_{cell}, cm^2	1.54
Parameter $\beta = b_h/b_w = \alpha_w/\alpha_h$	1/3 [28]

- The ASL effective hydrogen diffusivity can be correctly estimated from the fitted Warburg element provided that Eq. 40 holds.

Table IV. The anode parameters resulted from fitting of the analytical model to the experimental spectrum in Figure 6. The parameter indicated by asterisk has been fixed.

HOR Tafel slope b_h, mV / exp	107
HOR transfer coefficient $\alpha_h = RT/(b_h F)$	0.864
DL volumetric capacitance C_{dl}, F cm^{-3}	3.36
DL superficial capacitance $C_{dl,s}$, mF cm^{-2}	5.04
HOR exchange current density i_*, A cm^{-3}	355*
AAL ionic conductivity σ_i, mS cm^{-1}	1.65
ASL Knudsen H_2 diffusivity $D_{K,h}$, cm^2 s^{-1}	0.807
High–frequency resistance R_{HFR}, Ω cm^2	0.268
Ratio p_w^{ref}/p_h^{ref}	0.723
ASL porosity/tortuosity	0.0761
Cable inductance L_{cab}, nH	418

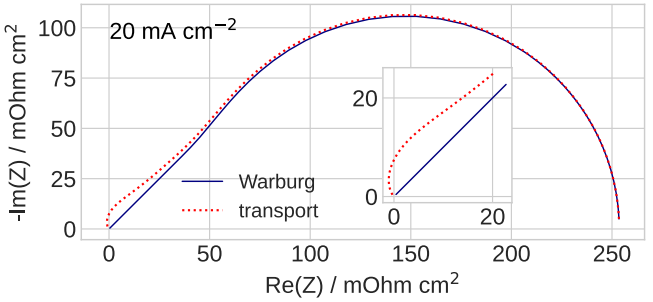

Figure 7. The Warburg finite–length impedance $Z_W/(qE_1)$, Eq. 35, (solid curve) and the transport impedance, Eq. 34, (dotted curve) calculated with the parameters from Table II. The inset shows the zoomed high–frequency part. The transport impedance exhibits a loop with $\mathrm{Re}(Z) < 0$ at high frequencies. However, since this impedance is connected in series with the faradaic and proton transport impedances, the real part of the full system impedance is always positive.

- The Warburg element distorts the high–frequency part of the spectrum, which may result in an incorrect value of the fitted active layer ionic conductivity.
- The validity of Eq. 30 is limited by Eq. A.3, which typically is much less restrictive than Eq. 40. Using Eq. 30 for fitting OCV and low–current spectra is thus much safer than using ECMs with the Warburg element.

Note that Eq. 40 was derived for the H_2–H_2O mixture. The presence of the third non-reacting component in the mixture (e.g. nitrogen) would increase the pressure gradient in the ASL. The higher pressure gradient would be required to achieve zero total flux of the non-reacting gas in the transport layer. Thus, in ternary systems, the condition Eq. 40 for neglecting the pressure gradient is necessary but not sufficient.

Last but not least, if the AAL is significantly more dense than the AAL, the finite pressure gradient could be developed in the AAL. If the cell current is small, the effect of $\partial p/\partial x$ on the hydrogen transport in the AAL can be estimated using Eq. 40 replacing the ASL thickness, L, with the AAL thickness, l_a, and the parameters y_c and p_c with their values at the ASL/AAL interface. Since the left side of Eq. 40 is proportional to l_a and l_a is two orders of magnitude smaller than L, we can expect Eq. 40 to hold meaning that the pressure gradient in the AAL can usually be neglected.

Conclusions

Analytical low-current and numerical high–current models for the anode impedance of an anode–supported button SOFC operated with neat hydrogen is developed. The models are based on the dusty gas transport model and they take into account the diffusive and the pressure–gradient driven transport of the hydrogen–water vapor mixture in the porous anode support layer (ASL). Numerical tests show that for the standard anode parameters, the analytical model, Eq. 30, works well up to the cell current density on the order of 20 mA cm^{-2}. The ASL transport resistivity is given by Eq. 37. We show that fitting the model which neglects the pressure gradient to an experimental spectrum may strongly underestimate the effective hydrogen diffusivity of the anode.

Fitting of the developed analytical model to the spectrum of a button–type SOFC measured at open circuit conditions returns a set of reasonable anode transport and kinetic parameters. The derived Eq. 30 for the anode impedance contains the ASL Knudsen hydrogen diffusivity, hydraulic permeability, porosity/tortuosity ratio, the active layer ionic conductivity, the DL capacitance and the HOR Tafel slope. Theoretically, all the aforementioned parameters could be obtained from fitting the model to experimental spectra. The analytical model reveals the pitfalls when fitting the equivalent circuit models with the Warburg finite–length element to the SOFC spectra. The more complicated numerical model can be used for fitting spectra measured at medium to high DC currents.

Appendix A. Derivation of the Analytical Impedance, Equation 30

If the DC current is small, the factors Y_1, P_1 and E_1 can be approximated by constant values. The terms $Y_1 y_1^1$, $P_1\tilde{p}_1^1$, E_1 in Eq. 26 and $\tilde{N}_1^1$ in Eq. 27 are thus independent of $\tilde{x}$. Here, Y_1, P_1 and E_1 are calculated setting $\tilde{p}^0 = \tilde{p}_c$, $y^0 = y_c$ in Eq. 24. Note that the perturbation amplitudes are still functions of $\tilde{X}$ (see below).

A good approximation of the overpotential $\tilde{\eta}^0$ can be obtained from the static charge conservation equation, Eq. 28, in the form

$$\varepsilon^2 \frac{\partial \hat{j}^0}{\partial \tilde{x}} = -q\tilde{p}_c\,(y_c \exp(\tilde{\eta}^0) - r_{ref}(1 - y_c)\exp(-\beta\tilde{\eta}^0)) \qquad [A\cdot1]$$

where $\hat{j}^0 = \partial\tilde{\eta}^0/\partial\tilde{x}$ is the local ionic current density. Assuming that the right side of Eq. A.1 is constant and integrating this equation over $\tilde{x}$ from 0 to 1, we get the current–voltage relation

$$J = l_a i_* q\tilde{p}_c\,(y_c \exp(\tilde{\eta}^0) - r_{ref}(1 - y_c)\exp(-\beta\tilde{\eta}^0)) \qquad [A\cdot2]$$

Equation A.2 is valid if the cell current density is small:[32]

$$J \ll \frac{\sigma_i b_h}{l_a} \qquad [A\cdot3]$$

For the set of active layer parameters in Table II, the right side of Eq. A.3 is 67 mA cm^{-2}, i.e., under given cell temperature, the equations of this section are valid up to the cell currents on the order of 10 mA cm^{-2}.

With this assumption, Eq. 26 is an ODE with the constant coefficients and the solution to Eq. 26 is

$$\tilde{\eta}^1(\tilde{x}) = \frac{\hat{j}^1 \cosh(\phi\tilde{x})}{\phi \sinh(\phi)} - \frac{q(Y_1 y_1^1 + P_1\tilde{p}_1^1)}{\mathrm{i}\tilde{\omega} + qE_1}, \quad \text{where}$$
$$\phi = \frac{1}{\varepsilon}\sqrt{\mathrm{i}\tilde{\omega} + qE_1} \qquad [A\cdot4]$$

The anode impedance is $\tilde{Z}_{anly} = \tilde{\eta}^1/\hat{j}^1|_{\tilde{x}=1}$ and since $\hat{j}^1 = \tilde{N}_1^1 J_*/j_*$, from Eq. A.4 we get

$$\tilde{Z}_{anly} = \frac{1}{\phi\tanh(\phi)} - \frac{\chi(Y_1 y_1^1 + P_1\tilde{p}_1^1)}{\tilde{N}_1^1(\mathrm{i}\tilde{\omega} + qE_1)}, \qquad [A\cdot5]$$

where χ is given in Eq. 31.

Further, at low DC currents, Eqs. 11, 13, 14 can be simplified. Setting $\partial\tilde{p}^0/\partial\tilde{X} = \partial y^0/\partial\tilde{X} = 0$, $\tilde{p}^0 = \tilde{p}_c$, and $y^0 = y_c$, from Eqs. 11,

13, 14 we get the reduced equations for the perturbation amplitudes $\tilde{N}^1$, $\tilde{p}^1$ and y^1:

$$\psi^2 \frac{\partial \tilde{N}^1}{\partial \tilde{X}} = -(\tilde{p}_c y^1 + y_c \tilde{p}^1) \mathrm{i}\tilde{\omega}, \qquad [A\cdot6]$$

$$(1 + \tilde{p}_c(3 - 2y_c)) \frac{\partial \tilde{p}^1}{\partial \tilde{X}} = 2\tilde{N}^1 \qquad [A\cdot7]$$

$$2\tilde{p}_c \frac{\partial y^1}{\partial \tilde{X}} + (1 + 2y_c + 3\tilde{p}_c) \frac{\partial \tilde{p}^1}{\partial \tilde{X}} = -2K\tilde{N}^1 \qquad [A\cdot8]$$

Equations A.6–A.8 form a system of linear ODEs with constant coefficients. This system with the boundary conditions Eq. 18 can be solved analytically. The solution is rather cumbersome and it is not displayed here. Setting $\tilde{X} = 1$ in the solutions we obtain the explicit formulas for $\tilde{N}_1^1$, y_1^1 and $\tilde{p}_1^1$, which appear in the second (transport) term in Eq. A.5. After some algebra, this gives the formula for the analytical impedance $\tilde{Z}_{anly}$, Eq. 30.

Appendix B. Transport Coefficients and the Dimensionless Parameters

The transport coefficients have been calculated as (Ref. 33)

$$B_0 = \frac{\lambda d^2}{32},$$
$$D_{K,h} = \frac{\lambda d}{3}\sqrt{\frac{8RT}{\pi M_h}}$$
$$D_m = \lambda D_m^{free} \qquad [B\cdot1]$$

where λ is the porosity/tortuosity ratio, d the mean pore diameter (Table II).

The first derivative of Eq. 15 over $\tilde{X}$ is given by

$$\frac{\partial y}{\partial \tilde{X}} = -\frac{W\tilde{p}_c y_c}{(\tilde{p}_c + W\tilde{X})^2} - \frac{6W\tilde{p}_c^2 + 2(3W^2\tilde{X} + 2K\tilde{J} + W)\tilde{p}_c + 3W^3\tilde{X}^2}{4(\tilde{p}_c + W\tilde{X})^2}. \qquad [B\cdot2]$$

ORCID

Andrei Kulikovsky https://orcid.org/0000-0003-1319-576X

References

1. A. Lasia, *Electrochemical Impedance Spectroscopy and its Applications* (Springer, New York) (2014).
2. S. Primdahl and M. Mogensen, "Gas diffusion impedance in characterization of solid oxide fuel cell anodes." *J. Electrochem. Soc.*, **146**, 2827 (1999).
3. A. Esquirol, N. Bonanos, N. Brandon, J. Kilner, and M. Mogensen, "Electrochemical characterisation of a $La_{0.6}Sr_{0.4}Co_{0.2}Fe_{0.8}O_{3-\delta}$ cahode for IT-SOFCs." *Proc. ECS*, **PV 2003–7**, 5802003.
4. R. Barfod, M. Mogensen, T. Klemensø, A. Hagen, Y.-L. Liu, and P. V. Hendriksen, "Detailed characterization of anode–supported sofcs by impedance spectroscopy." *J. Electrochem. Soc.*, **154**, B371 (2007).
5. V. Sonn, A. Leonide, and E. Ivers-Tiffée, "Combined deconvolution and CNLS fitting approach applied on the impedance response of technical Ni/8YSZ cermet electrodes." *J. Electrochem. Soc.*, **155**, B675 (2008).
6. A. Leonide, Y. Apel, and E. Ivers-Tiffée, "Sofc modeling and parameter identification by means of impedance spectroscopy." *ECS Trans.*, **19**, 81 (2009).
7. A. Kromp, H. Geisler, A. Weber, and E. Ivers-Tiffée, "Electrochemical impedance modeling of gas transport and reforming kinetics in reformate fueled solid oxide fuel cell anodes." *Electrochim. Acta*, **106**, 418 (2013).
8. J. Millichamp, T. J. Mason, N. P. Brandon, R. J. C. Brown, R. C. Maher, G. Manos, T. P. Neville, and D. J. L. Brett, "A study of carbon deposition on solid oxide fuel cell anodes using electrochemical impedance spectroscopy in combination with a high temperature crystal microbalance." *J. Power Sources*, **235**, 14 (2013).
9. J. Nielsen and J. Hjelm, "Impedance of SOFC electrodes: a review and a comprehensive case study on the impedance of LSM:YSZ cathodes." *Electrochim. Acta*, **115**, 31 (2014).
10. D. Macdonald, "Reflections on the history of electrochemical impedance spectroscopy." *Electrochim. Acta*, **51**, 1376 (2006).
11. W. Bessler, S. Gewies, and J. Warnatz, "Impedance simulations of SOFC patterned and cermet anodes from detailed electrochemical models." *Proc. Electrochem. Soc.*, **PV 2005-07**, 708 (2005).
12. H. Zhu and R. J. Kee, "Modeling elementary heterogeneous chemistry and electrochemistry in solid oxide fuel cells." *J. Electrochem. Soc.*, **153**, A1765 (2006).
13. W. Bessler adn S. Gewies, "Gas concentration impedance of solid oxide fuel cell anodes II. Channel geometry." *J. Electrochem. Soc.*, **154**, B548 (2007).
14. Y. Shi, N. Cai, C. Li, C. Bao, E. Croiset, J. Qian, Q. Hu, and S. Wang, "Simulation of electrochemical impedance spectra of solid oxide fuel cells using transient physical models." *J. Electrochem. Soc.*, **155**, B270 (2008).
15. P. Hofmann and K. D. Panopoulos, "Detailed dynamic solid oxide fuel cell modeling for electrochemical impedance spectra simulation." *J. Power Sources*, **195**, 5320 (2010).
16. W. Bessler, "Rapid impedance modeling via potential step and current relaxation simulations." *J. Electrochem. Soc.*, **154**, B1186 (2007).
17. A. Bertei, G. Arcolini, J. P. Ouweltjes, Z. Wuillemin, P. Piccardo, and C. Nicolella, "Physically-based deconvolution of impedance spectra: interpretation, fitting and validation of a numerical model for lanthanum strontium cobalt ferrite-based solif oxide fuel cells." *Electrochimica Acta*, **208**, 129 (2016).
18. A. Donazzi, S. D. Pascali, F. Garavaglia, and M. Bracconi, "A quasi 2D model for the interpretation of impedance and polarization of a planar solid oxide fuel cell with interconnects." *Electrochim. Acta*, **365**, 137346 (2021).
19. M. Knappe and A. Kulikovsky, "Analytical and numerical models for impedance of a button SOFC anode." *J. Electroanal. Chem.*, **975**, 118773 (2024).
20. Y. Shi, H. Wang, and N. Cai, "Direct two-dimensional electrochemical impedance spectra simulation for solid oxide fuel cell." *J. Power Sources*, **208**, 24 (2012).
21. Y. Fu, Y. Jiang, S. Poizeau, A. Dutta, A. Mohanram, J. D. Pietras, and M. Z. Bazant, "Multicomponent gas diffusion in porous electrodes." *J. Electrochem. Soc.*, **162**, F613 (2015).
22. A. Bertei, E. Ruiz-Trejo, F. Tariq, V. Yufit, N. P. Brandon, and A. Atkinson, "Validation of a physically-based solid oxide fuel cell anode model combining 3D tomography and impedance spectroscopy." *Int. J. Hydrogen Energy*, **41**, 22381 (2016).
23. A. Kulikovsky, "Dusty-gas model conservation law and approximate aanalytical solutions for H_2-H_2O transport in the SOFC anode support layer." *J. Electrochem. Soc.*, **172**, 014510 (2025).
24. E. Warburg, "Über das Verhalten sogenannter unpolarisirbarer Electroden gegen Wechselstrom." *Ann. Physik und Chemie*, **67**, 493 (1899).
25. A. Kulikovsky, "Why impedance of the gas diffusion layer in a PEM fuel cell differs from the Warburg finite-length impedance?" *Electrochem. Comm.*, **84**, 28 (2017).
26. Y. Shi, N. Cai, C. Li, C. Bao, E. Croiset, J. Qian, Q. Hu, and S. Wang, "Modeling of an anode-supported Ni-YSZ|Ni-ScSZ|ScSZ|LSM-ScSZ multiple layers SOFC cell. Part I. Experiments, model development and validation." *J. Power Sources*, **172**, 235 (2007).
27. C. Bao and N. Cai, "An approximate analytical solution of transport model in electrodes for anode–supported solid oxide fuel cells." *AIChE J*, **53**, 2968 (2007).
28. H. Zhu and R. J. Kee, "Modeling electrochemical impedance spectra in SOFC button cells with internal methane reforming." *J. Electrochem. Soc.*, **153**, A1765 (2006).
29. Y. Shi, N. Cai, C. Li, C. Bao, E. Croiset, J. Qian, Q. Hu, and S. Wang, "A general approach for electrochemical impedance spectroscopy simulation using transient mechanistic SOFC model." *ECS Trans.*, **7**, 1889 (2007).
30. Q.-A. Huang, M. Liu, and M. Liu, "Impedance spectroscopy study of an SDC-based SOFC with high open circuit voltage." *Electrochimica Acta*, **177**, 227 (2015).
31. A. Kulikovsky, "Analysis of proton and electron transport impedance of a PEM fuel cell in H_2/N_2 regime." *Electrochem. Sci. Adv.*, **1**, e202000023 (2020).
32. A. A. Kulikovsky, "The regimes of catalyst layer operation in a fuel cell." *Electrochim. Acta*, **55**, 6391 (2010).
33. A. Bertei and C. Nicolella, "Common inconsistencies in modeling gas transport in porous electrodes: The dusty-gas model and the Fick law." *J. Power Sources*, **279**, 133 (2015).